Surface & Coatings Technology 419 (2021) 127306

Contents lists available at ScienceDirect

Surface & Coatings Technology

journal homepage: www.elsevier.com/locate/surfcoat

Understanding the influence of microstructure on hot corrosion and erosion behavior of suspension plasma sprayed thermal barrier coatings

Nitish Kumar [a,*], Satyapal Mahade [a,*], Ashish Ganvir [b], Shrikant Joshi [a]

[a] University West, 46186 Trollhättan, Sweden
[b] Department of Materials and Mechanical Engineering, Faculty of Technology, University of Turku, 20014, Finland

ARTICLE INFO

Keywords:
Thermal barrier coatings
Suspension plasma spray
Erosion
Hot corrosion
Failure analysis
Damage mechanism

ABSTRACT

Thermal barrier coatings (TBCs) are bilayer systems comprising a 7–8 wt% yttria partially stabilized zirconia (YSZ) top coat deposited over a metallic bond coat. Suspension plasma spraying (SPS) is an advanced and attractive top coat processing technique due to its capability to yield a variety of microstructures, including the desired columnar microstructure for enhanced strain tolerance and durability. This work attempts to investigate the desirable microstructural features in an SPS processed TBCs to mitigate hot corrosion and minimize erosion related losses that are often responsible for coating degradation. SPS processed TBCs were deposited utilizing three different spray conditions to obtain distinct microstructural features (column density, interpass [IP] porosity bands, column width), porosity content, and mechanical properties. Apart from comprehensive characterization utilizing SEM, XRD and micro-indentation tests, the as-deposited TBCs were subjected to hot-corrosion tests in the presence of vanadium pentoxide and sodium sulfate as corrosive salts. Post-corrosion analysis revealed complete infiltration of the molten salts in all the investigated TBCs. However, the delamination cracks generated due to the infiltrated corrosive species were minimal in case of TBCs with higher fracture toughness. The differences in microstructure and mechanical properties also led to differences in erosion performance, with TBCs possessing minimal total porosity content and high fracture toughness best resisting erosion related damage. Post-erosion analysis revealed that the TBCs with higher fracture toughness and micro-hardness showed superior erosion resistance. Based on the erosion and corrosion results and subsequent post-mortem of failed specimens, plausible damage mechanisms are proposed. Findings from this work provide new insights on developing damage tolerant TBCs microstructures with enhanced durability when exposed to erosion and hot corrosion environments.

1. Introduction

Thermal barrier coatings (TBCs) are mainly used in the hot sections of gas turbine engines to provide thermal insulation to metallic components such as turbine blades and vanes [1]. The operating environment of the gas turbines severely affects the lifetime of the TBCs. The major performance criteria for TBCs in industrial gas turbines is excellent thermal shock lifetime and thermal cyclic fatigue lifetime [2] along with good thermal insulation [3]. However, hot corrosion and erosion of TBCs are the other major damage mechanisms that need to be considered for the design of durable TBCs [3].

Atmospheric plasma spraying (APS) and electron beam-physical vapor deposition (EB-PVD) are the two state of art techniques used to spray the ceramic top coat of TBCs. APS is capable of producing porous, lamellar microstructured TBCs (henceforth, the term 'TBC' will refer to the ceramic top layer), which possess low thermal conductivity [4], acceptable thermal cyclic lifetime [5] and, lower overall production cost compared to EB-PVD. On the other hand, EB-PVD processed TBCs possess dense columnar microstructure, which is believed to be highly strain tolerant, resulting in very high thermal cyclic lifetime [4]. However, EB-PVD processed TBCs have higher thermal conductivity [6] and the process is known to be an expensive one [7]. Therefore, this has motivated the desire to identify a TBC processing route that can exploit the merits of APS and EB-PVD processes. Suspension plasma spraying (SPS) is one such process that is capable of producing TBCs with columnar microstructure along with varied porosity scales at micron,

* Corresponding authors.
E-mail addresses: nitishkumar8123@gmail.com, nitish.kumar@hv.se (N. Kumar), satyapal.mahade@hv.se (S. Mahade), ashish.ganvir@utu.fi (A. Ganvir), shrikant.joshi@hv.se (S. Joshi).

https://doi.org/10.1016/j.surfcoat.2021.127306
Received 22 February 2021; Received in revised form 3 May 2021; Accepted 13 May 2021
Available online 19 May 2021

submicron, and nano-level [8]. SPS is a thermal spray technique based on APS process, wherein the traditional difficulties associated with feeding extremely fine powders are overcome by dispersing submicron particles in a suspension to facilitate their feeding to the plasma gun, and has received considerable research attention in recent times [9,10]. In general, different sections of a gas turbine engine need distinct TBC microstructures. SPS process is capable of producing TBCs with varied microstructural features (highly porous, feathery, inter pass (IP) porosity, columnar and dense vertically cracked), which can be realized by suitably altering the spray parameters and the suspension properties [4,11]. Such distinct microstructural features are difficult/impossible to achieve by employing conventional TBCs processing techniques such as APS or EB-PVD. Owing to their unique microstructures, SPS processed TBCs have shown performance benefits compared to the conventionally processed APS and EB-PVD TBCs in numerous prior studies. Recently, Bernard et al., Ganvir et al. and Zhao et al. demonstrated that, by tailoring the microstructure of SPS processed TBCs, lower thermal conductivity than APS and EB-PVD processed TBCs can be obtained [6,8,10]. Furthermore, Curry et al. reported excellent thermal shock resistance of SPS processed TBCs than the dense vertically cracked (DVC) TBCs [12], which is desirable to enhance the durability of engine components. Additionally, Lima et al. and Mahade et al. reported superior erosion resistance of SPS processed columnar microstructured TBCs than the APS and EB-PVD processed TBCs [13,14]. The above attributes of SPS technique have attracted industrial and scientific interest worldwide.

In terms of TBC failure mechanisms, erosion can be a major threat to TBCs durability [15], especially on the rotating components such as turbine blades. Erosion leads to significant loss of the ceramic top coat. In the past, numerous studies investigated the erosion behavior of TBCs processed by different routes. Nicholls et al. demonstrated that the EB-PVD TBCs have superior erosion performance as compared APS TBCs [16]. Similar results were obtained from the erosion test results performed by Cernuschi et al., where EB-PVD TBCs had higher erosion resistance than APS TBCs for the erosion test with erodent impact angle as 90°. However, the trend of erosion behavior of EB-PVD and APS TBCs was reversed when the impact angles were low (15° and 30°) [17]. Lima et al. studied the erosion behavior of SPS, EB-PVD and APS YSZ-based TBCs at 15° and 90° impact angles at room temperature. It was observed that the SPS TBCs exhibited higher erosion resistance than EB-PVD and APS TBCs [13]. Algenaid et al. investigated the erosion behavior of SPS TBCs with varied microstructure produced by utilizing six different suspension feedstocks and it was reported that the erosion performance of SPS TBCs is closely related to porosity content and fracture toughness [18]. Mahade et al. reported lower erosion resistance for APS processed TBCs than the columnar microstructured TBCs deposited by SPS and, attributed its improved erosion performance to the presence of columns [14]. Thus, SPS processed TBCs indeed show a promising potential with respect to mitigating erosion related losses, for being employed as TBCs on rotating components of gas turbine engines.

Another prominent TBCs damage mechanism is the molten salt attack (hot corrosion), which limits the longevity of TBCs used specifically in land-based gas turbines. YSZ is susceptible to molten salt attack at high temperatures (<1000 °C) due to selective leaching of yttria (stabilizer) from the YSZ, which often results in catastrophic failure due to undesirable phase transformation to monoclinic zirconia upon cooling [19,20]. There are two different, well investigated approaches in the literature to mitigate molten salt infiltration in TBCs. The first approach relates to utilizing alternative top coat compositions (such as pyrochlores, perovskites etc.) as YSZ is susceptible to molten salt attack [21]. The second approach is to tailor the TBCs microstructure to mitigate molten salt infiltration [22]. Batista et al. reported improved hot corrosion performance of TBCs by employing a post processing technique such as laser glazing to densify the top surface that resisted molten salt infiltration [23]. Mahade et al. reported a denser, sacrificial top surface yttria layer in a multi-layered TBC [24]. The purpose of this denser yttria layer is to act as a reservoir of yttria rich phase in order to combat hot corrosion, however it could not help to prevent the molten salt attack due to its discontinuity at the column gaps [24]. As discussed previously, the erosion resistance of TBCs is also dictated by the top coat composition and microstructure [25,26]. Najafi et al. compared hot corrosion behavior of state-of-the-art APS and two compositionally different zirconia (8YSZ and 48YSZ) based SPS TBCs [27]. It was reported that 48 YSZ SPS TBCs had lower molten salt infiltration depth compared to 8YSZ due to higher yttria content in 48YSZ than 8YSZ, which provided adequate supply of Y^{+3} ions that interacted with the molten salt and mitigated further salt infiltration. In general, it can be said that the hot corrosion and erosion resistance of the TBC is intimately linked to its microstructure. The goal of this work is to investigate the influence of a specific set of microstructural features in SPS processed TBCs such as column density, column width coarse porosity content (from column gaps) etc. on the fracture toughness, erosion performance and hot corrosion resistance. Thirumalaikumarasamy et al. demonstrated that process parameters such as input power, spray distance, powder feed rate etc. are critical for tailoring APS microstructure by optimizing porosity content [28]. Studies like these have helped to develop reliable APS TBCs, thus motivating the need for a similar research effort on the development of SPS processed TBCs. In this study, three different SPS processed YSZ TBCs were deposited by utilizing different spray distance, suspension feed rate, total gas flow, as well as plasma power and enthalpy. The rationale for opting these spray conditions was that, in our previous work [8,29], TBCs manufactured utilizing these spray conditions demonstrated conflicting rankings in terms of desirable TBC performance attributes (thermal insulation and thermal shock lifetime). Although the study may appear to cover a narrow range of microstructural variations, it is clear that the parametric window investigated yields distinctly different columnar TBCs with substantially varying column widths and inter-columnar spacing. All of these can lead to significant differences in coating performance [4]. As such, it is both educative and relevant to also closely examine the influence of the above microstructural differences on erosion and corrosion behavior. The deposited TBCs were characterized for their microstructure (column density, pore size, column width etc.), phase composition, porosity, hardness etc. and later subjected to erosion and hot corrosion tests. Post-erosion and post-corrosion analysis of the tested TBCs was performed to gain further insights on their damage mechanisms. The differences in microstructural features of the deposited TBCs were correlated with the erosion and corrosion results, and plausible erosion and corrosion mechanisms are also proposed.

2. Experimental work

2.1. Sample preparation

Hastelloy-X substrates of 25.4 mm diameter and 6 mm thickness were grit blasted using alumina powder (220 grit size) to a surface roughness Ra of approximately 3 μm before bond coat deposition. Commercially available CoNiCrAlY powder (AMDRY 9951, Oerlikon Metco, Wohlen, Switzerland) was then sprayed on the substrate using an M3™ supersonic high velocity air fuel (HVAF) spray torch (UniqueCoat, Richmond, USA) to obtain a bond coat thickness of 200 μm ± 15 μm. 8 wt% yttria stabilized zirconia (8YSZ) (INNOVNANO, Coimbra, Portugal), in the form of a suspension was used as the feedstock for depositing the insulating top coat. The suspension had a solid load of 25 wt% 8YSZ in ethanol with a particle size distribution of $D_{10} = 100$ nm, $D_{50} = 500$ nm and $D_{90} = 1$ μm. The 8YSZ top coat was sprayed using an Axial III high power plasma torch equipped with a Nanofeed 350 suspension feed system (Northwest Mettech Corp., Vancouver, Canada) to obtain a top coat layer thickness of approximately 250–300 μm. Three different sets of parameters were used to spray the YSZ top coat layers on identically bond coated substrates. The parameters used in this study were chosen based on a previous investigation carried out in the authors'

group [4]. The spray parameters utilized to deposit the YSZ TBCs are shown in Table 1, along with the corresponding nomenclature (C1–C3) used for the resulting TBCs.

2.2. Erosion testing

Erosion tests were conducted on all the three as-deposited SPS TBC samples as per the ASTM G76 standard. The erosion tests were performed using an air jet erosion test machine (TR-470, Ducom Instruments, India) at an impingement angle of 90°. Prior to each test, the erodent media was placed in a furnace operating at 100 °C for 24 h to remove any moisture, which could otherwise lead to agglomeration of the particles and clogging of the test rig nozzle. The distance between the nozzle and the surface of the coated sample was kept at 10 mm. The erosion test parameters are shown in Table 2. Three coupons of each TBC variation were utilized for the erosion tests. Five independent erosion tests were performed on each TBC specimen and the weight loss was measured using a sensitive weighing machine (PCE Instruments AB100, Southampton, United Kingdom). The specimens were ultrasonically cleaned every time before measuring the weight loss to prevent any loosely bound erosion debris to influence the weight loss measurements. Five erosion indents were made on each specimen from the three SPS TBCs. Post-erosion, both the top surface and the cross-section of each erosion pit were analyzed. The top surface analysis included 3D topography of the erosion pit and the top view SEM micrographs. Thickness loss was measured using white light interferometry with Profilm3D (Filmetrics Europe GmbH, Germany). In order to validate the weight loss results, erosivity number was calculated along with erosion rate using Eqs. (1) and (2).

$$Erosivity\ number = \frac{time\ of\ exposure\ in\ \mathrm{s}}{thickness\ loss\ in\ \mathrm{mils}} \quad (1)$$

$$Erosion\ rate = \frac{weight\ loss\ of\ coating\ in\ \mathrm{g}}{mass\ of\ erodent\ used\ in\ \mathrm{kg}} \quad (2)$$

2.3. Corrosion test

Corrosion tests were conducted on one specimen from each of the SPS TBC variants using a mixture of vanadium pentoxide (V_2O_5) and sodium sulfate (Na_2SO_4) in the ratio 55:45 wt%. For the hot corrosion test, 2 specimens from each TBC variation were utilized. Both the salts (V_2O_5 and Na_2SO_4) were manually crushed and mixed in a ceramic bowl for homogenizing the salt mixture. A salt concentration of approximately 4.4 mg/cm^2 was applied manually on the TBC surface. The specimens were later placed in an electric furnace for 8 h at a test temperature of 900 °C. After 8 h, the specimens were left to cool in the furnace to room temperature, in order to avoid thermal shock to the TBCs.

2.4. Microstructure characterization

Standard metallographic procedures, as discussed in detail in our previous work [30], were utilized to prepare the specimens for further analysis. The top view and cross section micrographs of the as-deposited TBCs, pits resulting from erosion testing (described below) and the corroded specimens were analyzed using a scanning electron microscope (SEM) (HITACHI TM3000, Japan). The thickness of TBCs was determined in Microsoft Paint (MS Paint) by utilizing ten independent cross-sectional SEM micrographs. The elemental analyses on the corroded TBCs were carried out using Energy-dispersive X-ray spectroscope (EDS) (Bruker, Germany).

Table 2
Erosion test parameters.

Parameters	Set
Erodent	Alumina
Grit size (μm)	50 ± 20
Particle velocity (m/s)	30 ± 2
Flow rate (g/min)	2 ± 0.25
Exposure time (s)	45
Impact angle (°)	90

2.5. Porosity analysis

The porosity in the as-deposited TBCs was measured using two different techniques, namely, Image analysis technique and mercury infiltration porosimetry (MIP), since SPS TBCs have an inherently wide pore size distribution. As the image analysis technique has been reported to under-predict the fine scale porosity (sub-micron and nano sized pores) [8,29], the MIP technique was chosen to quantify the fine scale porosity. Thus, a combination of image analysis and MIP technique was used to analyze the total porosity content in TBCs. The porosity in the TBCs was characterized into four different classes of porosity, as explained in detail in Section 3.2. Image analysis was used to determine class 1 and class 2 pores whereas class 3 and class 4 pores were determined by MIP technique. The MIP measurements were carried out on free standing ceramic top coats. All the coated specimens were first cut into a rectangular sample (10 mm × 24 mm) and then immersed in a solution containing a mixture of nitric acid and hydrochloric acid in 1:3 volume ratio for a time period of 1 h to produce free standing ceramic top coats [32]. Image analysis was used to quantify coarse porosity in the ceramic top coat using a public domain, Java-based image processing software ImageJ [31]. The detailed procedure adopted for porosity measurement is discussed elsewhere [4].

2.6. XRD analysis

The top surfaces of corroded and as-deposited TBC samples were examined by XRD phase analysis in the 2-theta range of 20 to 40° using X'pert Pro (PANalytical, Malvern, United Kingdom). Cu K_α of wavelength 1.54 Å was used at slow scan rate (step size of 0.01° and time per step of 10 s). The peaks obtained after the analysis were identified and labelled using JCPDS standard.

2.7. Column density measurement

The column density in each case was measured using 5 SEM micrographs captured at a magnification of 200× over the entire cross-section of the TBC. A straight line was drawn at the middle of ceramic top coat layer thickness and the length of the resulting line was measured in micrometers. All the column boundaries that intersected the line that was drawn, were counted. The column density (columns/mm) was then calculated, using Eq. (3) [12]:

$$column\ density = \frac{(No.of\ column\ boundaries\ intersecting\ the\ line - 1)}{True\ length\ of\ the\ line} \quad (3)$$

Table 1
Plasma spray parameters utilized to spray the TBCs.

TBC	Spray distance (mm)	Suspension feed (ml/min)	Total gas flow (l/min)	Power (kW)	Enthalpy (kJ)	Coating thickness (μm)	Deposition rate (μm/pass)
C1	100	45	300	108	7	273 ± 24	1.4 ± 0.1
C2	75	70	250	119	11.1	248 ± 16	3.3 ± 0.2
C3	75	100	300	142	12.4	305 ± 18	7.6 ± 0.4

2.8. Mechanical properties

E-modulus and micro-hardness of the ceramic top coat were experimentally calculated using a computer controlled micro-indenter equipment (H100, Fischerscope, Helmut Fischer GmbH, Germany). Fracture toughness measurements were carried out using a Vickers indenter (Shimadzu HMV-2 T Microhardness Tester). All the measurements were carried out on polished cross-section of TBCs. A total of 25 indents comprising of a square pyramidal shape indenter, were made to create cracks in the TBC. All the indents were made at the center of the columns. The cracking pattern was identified as Palmqvist cracks. Eq. (4) was used to calculate the fracture toughness of as-deposited TBCs [33].

$$K_{IC} = 0.018\left(\frac{E}{H_{IT}}\right)^{\frac{2}{5}} H_{IT} a^{\frac{1}{2}} \left(\frac{a}{l}\right)^{\frac{1}{2}} \quad (4)$$

where K_{IC} is the mode I indentation fracture toughness (MPa·m$^{1/2}$), E is the elastic modulus (MPa), a is the indentation half-diagonal length (m) and l is the crack length (m). A detailed description of the fracture toughness measurements is described in our previous work [4].

3. Results & discussion

3.1. Microstructure analysis

The cross-sectional SEM micrographs of the as-deposited SPS TBCs at low and high magnification are shown in Fig. 1. It can be observed that, although all the three TBCs have a columnar microstructure, they possess distinct microstructural features. In particular, the nature of columns (column density, column width etc.) in each of the TBCs seems to be distinct from the others. It can be observed that C1 has an open column like microstructure with greater column gaps as compared to relatively compact columns in C2 and C3. The darker areas in C1 correspond to column gaps, which also include partially molten particles. From high magnification cross-sectional SEM micrographs shown in Fig. 1, apart from coarse and fine scale porosities, IP porosity bands were observed in case of C3, as indicated by the yellow dotted line in Fig. 1(c). IP porosity bands can be regarded as weak links in the top coat layer, since they can promote horizontal crack propagation, as discussed further in Section 3.2. On the other hand, these IP porosities in a TBC can lower the thermal conductivity. The column densities and column widths measured for the SPS TBCs are depicted in Fig. 2. It can be noted that C1 showed greater column density followed by C2 and C3. It has been reported that the column formation is influenced by both the suspension properties (surface tension, viscosity, density etc.) as well as the plasma spray parameters (power, enthalpy, gas flow, spray distance etc.) [34]. The difference in the column density can be explained by the difference in the droplet momentum due to different parameters used during the spraying. The higher spray distance in combination with lower suspension feed rate, power and enthalpy imparts lower momentum to the particles [4].

When the solvent evaporates from the suspension droplet after being exposed to the plasma, the particles deposit either as well-molten splats or partially molten particles. Hotter plasma parameters can result in complete melting of particles, which can form typical pancake shaped splats. Formation of such splats can lead to better cohesion, resulting in better mechanical properties of the TBC, as discussed in Section 3.3. The available energy in the plasma plume as well as the dwell time of the particles in it play a crucial role and are responsible for formation of contrasting microstructures in the TBC. The dwell time of particles is governed by several parameters like suspension feed rate, spray distance and total gas flow, while the plasma power and enthalpy are indicators of available energy in the plasma plume [4]. In case of C1, a higher spray distance in combination with lower power and enthalpy was used. All these factors could lead to inadequate melting of particles to be deposited as fused splats, which leads to fine-scale porosity in the TBCs [35]. The partially-molten particles in case of C1 can be seen in Fig. 1, shown by the red arrow mark. On the other hand, the parameter for C3 had a reduced spray distance along with higher available energy, resulting in lesser number of partially-molten particles being incorporated in the TBC.

3.2. Porosity

Fig. 3 illustrates the porosity content in all the three types of TBCs

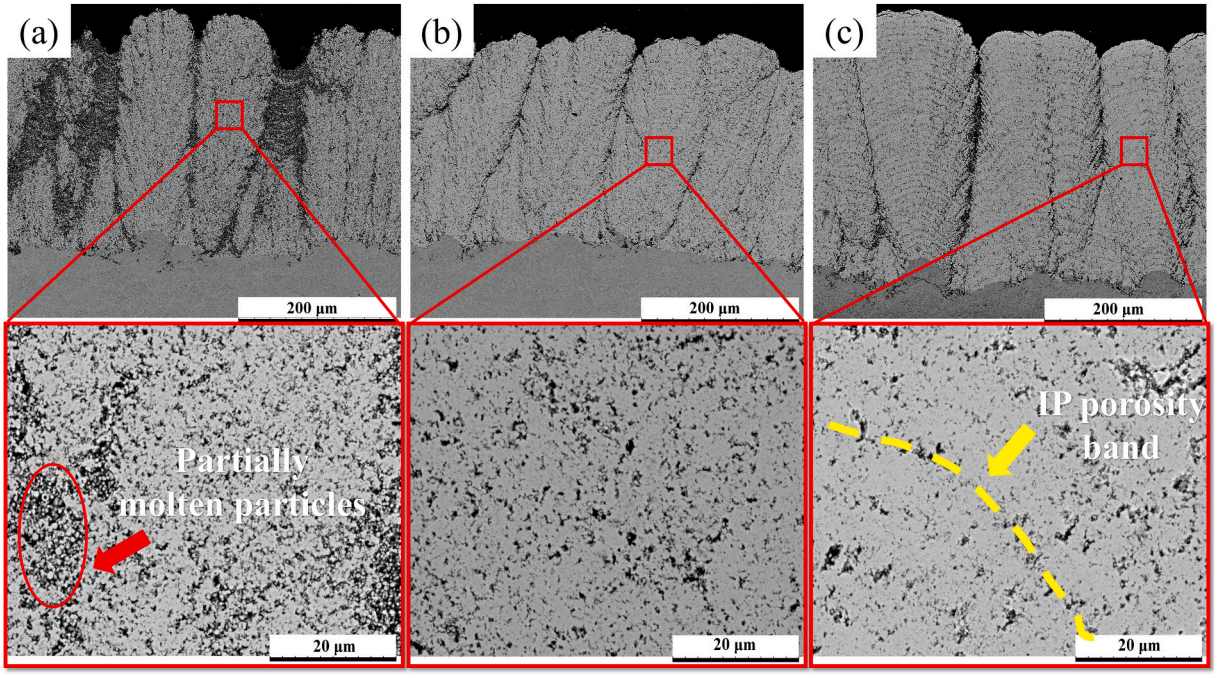

Fig. 1. As-deposited cross section SEM micrographs at low and high magnifications (a) C1, (b) C2, (c) C3.

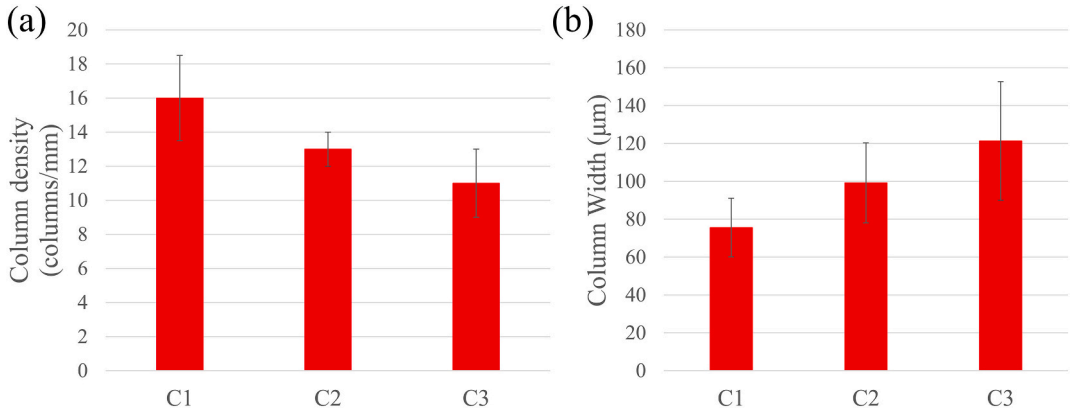

Fig. 2. (a) Column density and (b) column width of the TBCs.

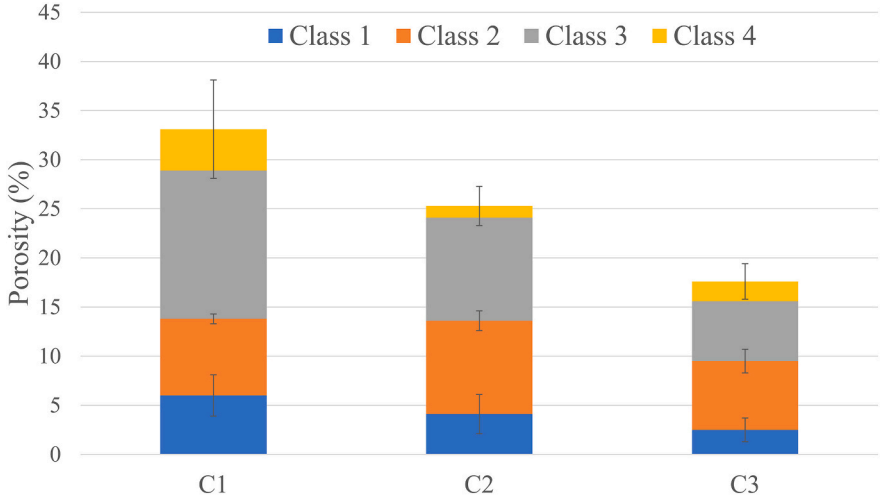

Fig. 3. Different classes of porosity content in TBCs.

studied. The porosity of the TBCs was quantified in four different classes based on pore size (diameter), Class 1 (>10 μm), Class 2 (10 μm–1 μm), Class 3 (1 μm–100 nm) and Class 4 (<100 nm), consistent with a previous study from this group [4]. Such a classification was done to differentiate the large (>10 μm) as well as micron/sub-micron/nano sized pores and study their individual role on coatings' performance. It is important to highlight that column gaps and cracks are the primary contributors to the class 1 and class 2 porosity whereas the class 3 and class 4 pores are mainly present within the columns. The total porosity of the TBCs was determined by summing up all the four porosity classes. The TBCs, C1 and C2 were found to have a highly porous microstructure with total porosity values of 33% ± 5 and 26% ± 2, respectively. This can be attributed to the spray parameters that were used. As discussed in earlier section, low enthalpy and low power were used in combination with higher spray distance in case of C1, which explains the higher porosity value obtained. The column gaps also contribute to the coarse porosity in the TBC. Greater the column density, greater would be the inter-columnar gaps, which in turn contributes to the coarse porosity content in the deposited TBCs Additionally, another distinctive microstructural feature among the investigated TBCs is the presence of IP porosity bands in C3, as shown in Fig. 1 by the yellow arrow. During spraying, the particles that are at the periphery of plasma plume, which is colder than the plume core, are poorly treated and deposit as semi-molten or partially molten splats due to lack of sufficient thermal energy, thus resulting in porous regions [4]. Incorporation of some unmolten particles in the coating, along with the well-molten splats, is inevitable. The source for the former is often the suspension droplets that travel along the periphery of the plasma jet. The well-melted particles that were treated at the warmer plume core deposit as fully molten splats [4]. When superimposing passes, IP porosity bands are generated as the partially-molten splats are sandwiched between molten splats. This can be attributed to the relatively higher rate of material deposition per pass in C3 compared to other two TBCs. As can be noted from Table 1 that the material rate deposition was more than double the C1 and about seven-fold higher than C2. With repeated passes of the plasma torch, the above undesired unmolten particles continue to get deposited and serve as the source for formation of porosity bands. The possibility of formation of such porosity bands is particularly high when high material deposition rate per pass is used for coating formation as in case of C3. These IP porosity bands mainly correspond to class 3 and class 4 porosity. The generation of such IP porosity bands can be directly linked to the traverse of the plasma gun [36]. Additionally, in the case of C3, the power and enthalpy of the plasma were relatively higher, resulting in greater degree of feedstock melting, which results in lower porosity compared to the other two TBC variants. Different porosity classes plausibly influence the overall erosion and corrosion performance of the coatings in varied ways. For instance, class-1 and class-2 porosity were the degradation initiation sites under both erosive as well as corrosive conditions. On the other hand, the class 3 and class 4 pores promote crack propagation through the column when subjected to erosion. Similarly, when subjected to molten salt attack, the class 1 and class 2 porosity provide an easier infiltration path. On the other hand, class 3 and class 4 porosity facilitate salt infiltration only if the pores are interconnected. For example, pore classes 3 and 4 become relevant (molten

salt infiltration) in case of coating C3, which comprises IP porosity bands.

3.3. Mechanical properties

The fracture toughness and micro-hardness values of the TBCs are shown in Fig. 4. It can be observed that the fracture toughness of C2 and C3 was similar, whereas C1 yielded the lowest fracture toughness value (1.58 ± 0.03 MPa·m$^{0.5}$) when compared to C2 (1.72 ± 0.03 MPa·m$^{0.5}$) and C3 (1.73 ± 0.03 MPa·m$^{0.5}$). The porosity ranking, as shown in Fig. 3, was inverse to the hardness and fracture toughness ranking depicted in Fig. 4. It should be mentioned that the TBC porosity content has a direct correlation with the mechanical properties, where higher porosity content generally results in inferior mechanical properties, for identical TBC compositions [37]. Furthermore, the mean hardness values of C2 and C3 were found to differ significantly although their fracture toughness values were similar. As pointed out in an earlier study [4], the fracture toughness is governed by class 1 and class 2 pores which act as crack initiation sites due to the higher stress intensity factors resulting from these pore classes compared to class 3 and class 4. As seen in Fig. 3, the class 1 and class 2 porosity levels were similar in C2 and C3, which could have been the reason for similar fracture toughness being measured in these coatings. On the other hand, the difference in class 3 and class 4 porosity for C2 and C3 was significant, which could have led to the difference in hardness in these TBCs. The IP porosity bands were found to have an influence on TBC performance in terms of erosion and corrosion behavior. For instance, compared to C1 and C2, the presence of IP porosity bands in C3 contributed to overall porosity in addition to the column gaps and porosity within the columns. However, despite their presence, the hardness and fracture toughness of C3 was higher compared to both C1 and C2. As pointed out earlier, these porosity bands belong to the finer class of porosity i.e., class 3 and class 4. It can be postulated that the larger sized porosity i.e., class 1 and class 2, could have been the primary porosity class governing hardness and fracture toughness in the coating and the performance as they favor crack propagation with relative ease. This was also shown in a previous study [4], where the larger pores resulted in a higher stress intensity factor that promotes crack initiation. On the other hand, the IP porosity bands could assist in inducing horizontal cracks in TBCs.

It should be mentioned that the micro-indentation technique employed in this study represents localized fracture toughness of the TBC, as the indents were made preferentially within the column and the column gaps were deliberately avoided. The alternative fracture toughness evaluation techniques such as the flexural test (3 point and 4 point bending test), which provide global fracture toughness of the coating, have been employed for lamellar microstructured TBCs processed by APS [38,39]. However, challenges in employing such techniques for fracture toughness evaluation in a columnar microstructured TBC is that the pre-existing 'cracks' (column gaps) in the TBC formed during its processing stage accelerates crack propagation and results in unreliable measurements. Therefore, it is challenging to evaluate fracture toughness of a columnar microstructured TBC due to the inherent heterogeneity in features. Despite the drawbacks of micro-indentation technique, it is widely employed by several research groups to evaluate the fracture toughness of columnar microstructured TBCs [40,41] due to the fact that it provides a reasonable relative comparison among the investigated TBCs. Therefore, the fracture toughness results presented in this work should also be interpreted as an indicative relative measure rather than being trusted for absolute values.

3.4. Erosion performance

The erosion performance of the SPS TBCs was assessed based on the erosion rate and erosivity number determined as described previously in Section 2.2 and shown in Fig. 5.

3.4.1. Erosion rate and erosivity number

C1 showed the highest erosion rate among all the investigated TBCs whereas the erosion rate of C2 and C3 were comparable and lower than C1 by a factor of almost ½, according to Fig. 5. Furthermore, to validate the erosion rate results, the erosivity number was also evaluated. The Erosivity number does not have error bars because, during post-erosion analysis, only one erosion pit was captured in each case (C1, C2 and C3). The thickness loss post-erosion in the investigated TBCs was measured using cross-sectional SEM micrographs. From Fig. 5(b), it can be observed that C3 showed the highest erosivity number whereas C1 showed the lowest. Higher erosivity number indicates higher erosion resistance. The erosion rate and erosivity number results indicate that C3 was the most erosion resistant among the three TBCs investigated whereas C1 was relatively more prone to erosion. There are several factors influencing the erosion performance of TBCs, such as microstructure, porosity content, and fracture toughness [8]. Higher fracture toughness allows more kinetic energy of the erodent to be absorbed by the TBC before the onset of delamination cracks. The above erosion results are in agreement with the literature [18,26], with the lower fracture toughness in C1 being plausibly responsible for its inferior erosion resistance. On the other hand, the superior erosion resistance of C3 can be attributed to its lower porosity content, higher hardness, and higher fracture toughness. Although C2 and C3 showed comparable fracture toughness, the relatively higher hardness and lower porosity content in C3 compared to C2 could have resulted in slightly higher erosion resistance of the former. Similar observations on erosion resistance of gadolinium zirconate-based TBCs processed by SPS were also made by Mahade et al. [26].

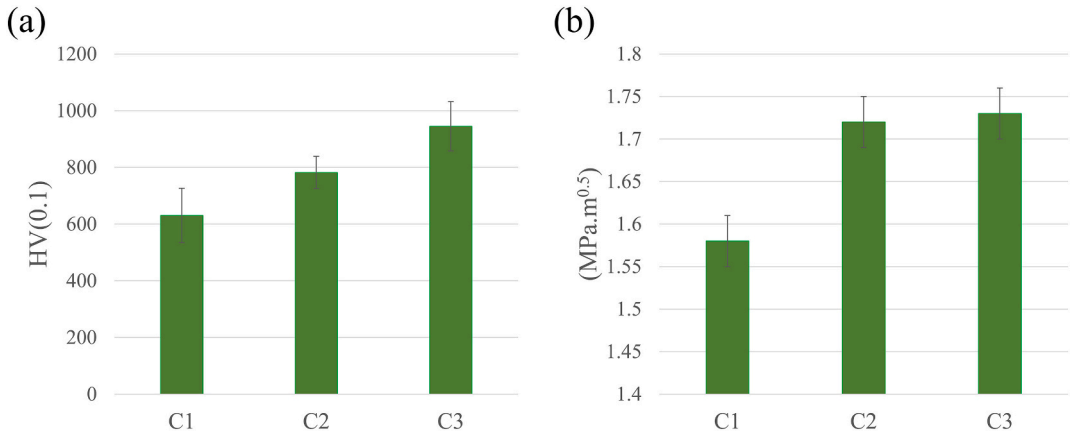

Fig. 4. (a) Micro-hardness and (b) fracture toughness of TBCs.

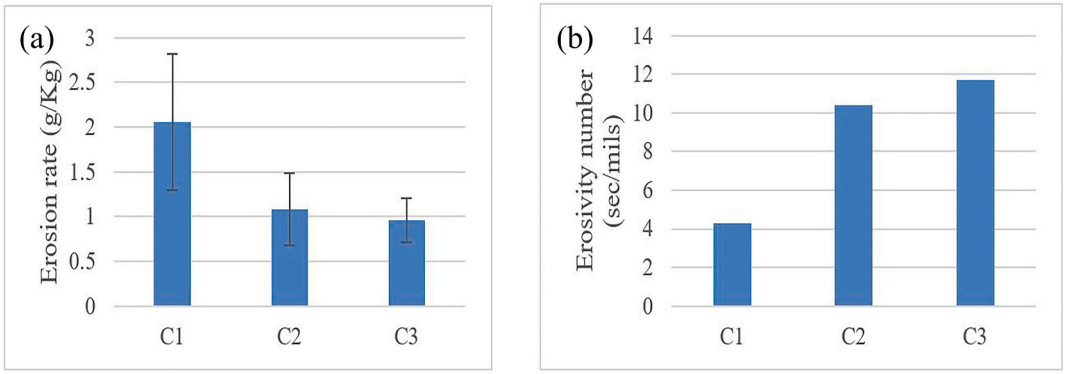

Fig. 5. (a) Erosion rate and (b) erosivity numbers of TBCs.

3.4.2. Post-erosion SEM analysis

The SEM micrographs (top surface and the cross-section) of the eroded TBCs are shown in Fig. 6. From the top view SEM micrographs shown in Fig. 6(a), (b) and (c), the eroded area was approximately 1.5 mm in diameter and more localized in the case of C1, as compared to C2 and C3. It should be mentioned that the exit nozzle dimension of the erosion test rig was 1.5 mm. The C1 TBC, upon erodent impact, seems to collapse/tunnel through the porous microstructure. Tunneling is an erosion-based failure mechanism in TBCs, which typically results in higher material removal in a ceramic [42]. As the erodent with sufficiently high kinetic energy impacts on the surface of the TBC, the tunneling occurs via defects in the microstructure (pores) and causes higher material loss. On the other hand, C2 and C3 resisted such localized collapse/tunneling via defects (pores), and instead, the material loss was due to splat fracture at the column heads. This type of erosion related damage mechanism in SPS TBCs could be described as "light ablation" [13]. In the cross-sectional SEM micrographs of C1, C2 and C3, it can be seen that the material loss was maximum in case of C1, from Fig. 6(a-1), (b-1) and (c-1), i.e., major portion of the columns seems to have eroded in case of C1. The degree of damage in C2 and C3 was less severe as compared to C1, as major portions of the columns were still visible after erosion. The near-surface delamination cracks at higher magnification SEM micrographs are also clearly evident in the investigated TBCs. The cross-sectional SEM results concur with the top surface results, with the loss in material appearing localized in case of C1 due to collapsing/tunneling mechanism of erosion. This could be attributed to

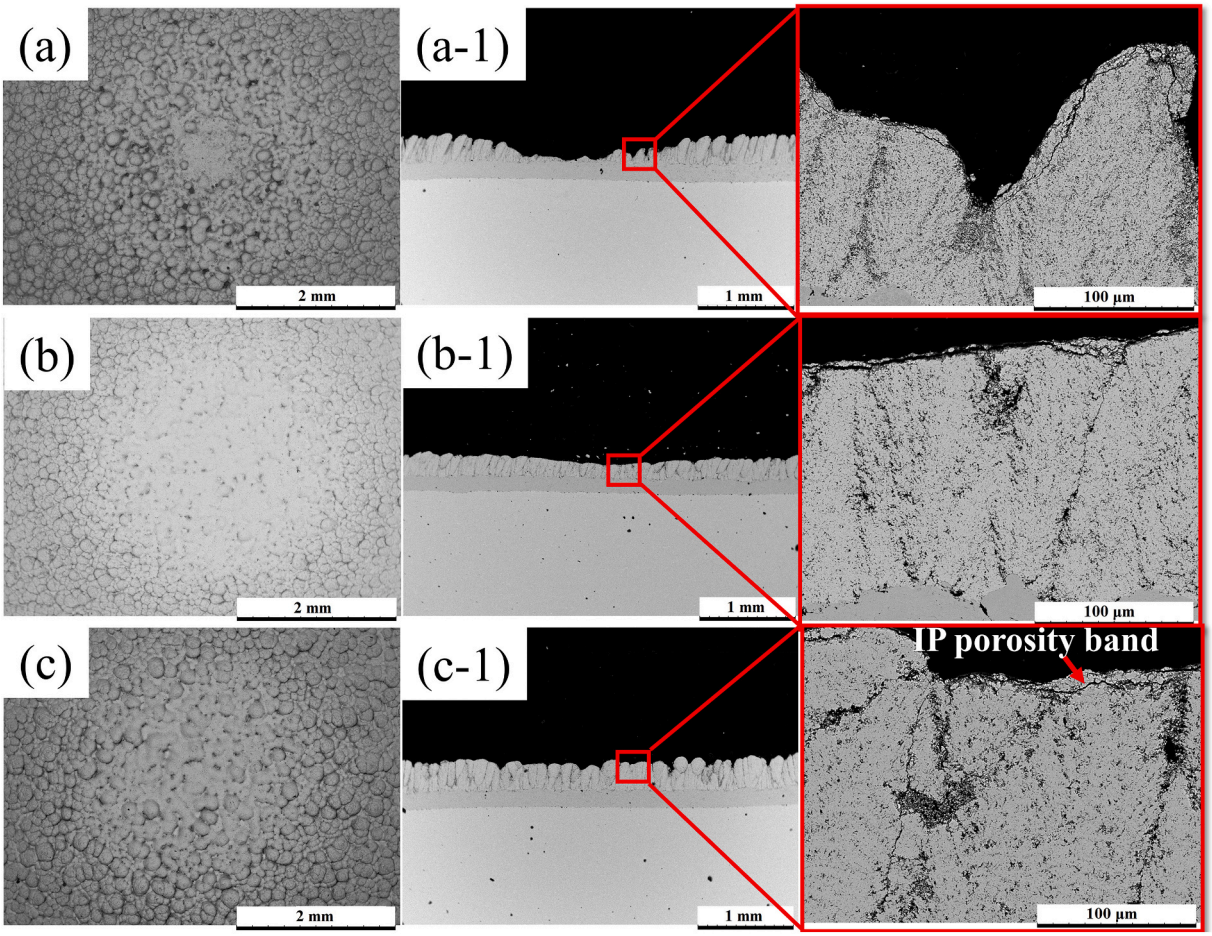

Fig. 6. SEM micrographs of eroded TBCs showing top view of (a) C1, (b) C2 and (c) C3 along with cross section of (a-1) C1, (b-1) C2 and (c-1) C3.

the relatively higher column density in the case of C1, where the column gaps contributed to higher coarse porosity content, which favored tunneling erosion mechanism and resulted in maximizing the material loss. Similar findings were reported by Wellman et al. for EB-PVD TBCs, where the coarse porosity regions favored crack initiations compared to fine porosity regions [25]. Therefore, it could be said that the presence of coarse porosity in a TBC is detrimental to its erosion resistance. These findings are in agreement with a recent study where higher unmolten splats in plasma sprayed TBCs, which resulted in high local porosity, were shown to be the weak link in the microstructure as they favored tunneling erosion mechanism [43]. The presence of IP porosity bands can favor material removal in TBCs during erosion, as they provide an easier pathway for horizontal crack propagation. In this work, the erosion exposure duration for all the investigated TBCs was finalized when two conditions were fulfilled: a) the erosion loss was restricted within the ceramic top coat without exposing the bond coat b) a measurable weight loss due to erosion was noted in all the TBCs. Therefore, it should be highlighted that the due to the erosion test conditions employed (low exposure time), it is plausible that only the subs-surface IP porosity bands accelerated material removal. In addition to the nature of pores, mechanical properties such as hardness and fracture toughness influence the erosion results, where TBCs with higher hardness and fracture toughness possess higher erosion resistance [26].

3.4.3. Erosion mechanism

Based on the obtained erosion results and post erosion analysis, the erosion mechanism of the SPS TBCs have been proposed, see Fig. 7. In case of C1, the open column-like microstructure with higher column density and column gaps along with inferior fracture toughness, is more prone to erosion by tunneling mechanism, which results in maximum material loss, as depicted in Fig. 7. On the other hand, due to the compact column-like microstructures for C2 and C3, along with relatively higher fracture toughness, the TBCs possess relatively superior erosion resistance, as illustrated in Fig. 7.

3.5. Corrosion performance

The top view SEM micrographs of the corroded SPS TBCs along with EDS maps are presented in Fig. 8. The higher magnification SEM micrographs in Fig. 9 show rod-shaped structures on the surface that correspond to the corrosion products formed due to the chemical interaction of the molten salts (V_2O_5 and Na_2SO_4) with YSZ layer. EDS map revealed the needle-like corrosive products on the TBCs comprised elements Y and V. XRD and EDS analysis revealed that the needle –like phases observed in all the TBCs after corrosion correspond to YVO_4.

A similar corrosion product for 8YSZ TBC has been reported in the literature when exposed to identical molten salt composition [44]. These corrosion products form due to the following reactions [39–45].

$$V_2O_5 + Na_2SO_4 \rightarrow 2\,NaVO_3 + SO_3 \quad (5)$$

$$ZrO_2\,(Y_2O_3) + 2\,NaVO_3 \rightarrow ZrO_2\,(\text{monoclinic}) + 2\,YVO_4 + Na_2O \quad (6)$$

Y_2O_3 can also directly react with V_2O_5 to form YVO_4 [52],

$$ZrO_2\,(Y_2O_3) + V_2O_5 \rightarrow ZrO_2\,(\text{monoclinic}) + 2\,YVO_4 \quad (7)$$

When the molten salt reacts with YSZ, it results in the formation of YVO_4 and ZrO_2 (monoclinic), according to the above equations. The phase transformation from Tetragonal (t′) to monoclinic (m) phase of zirconia is associated with high volume change (expansion), generating additional stresses in the top coat [44]. This could also contribute to premature failure of the TBC. The XRD analysis of the corroded region (Fig. 12) confirms the presence of monoclinic zirconia.

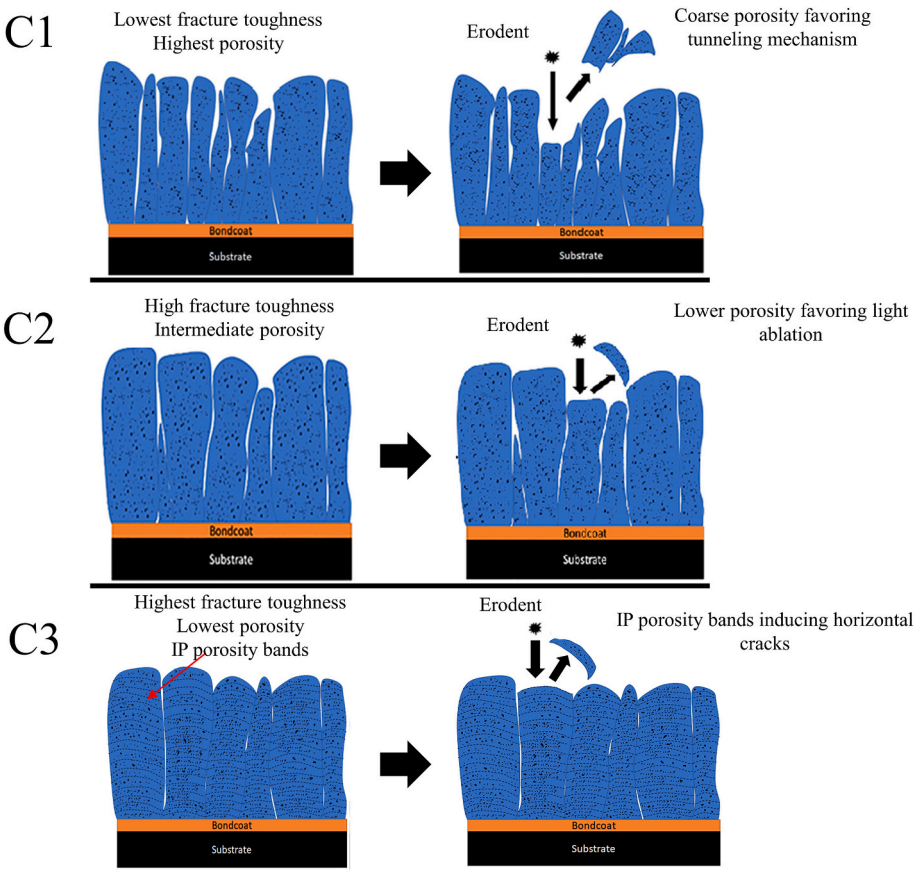

Fig. 7. Proposed erosion mechanism of the TBCs.

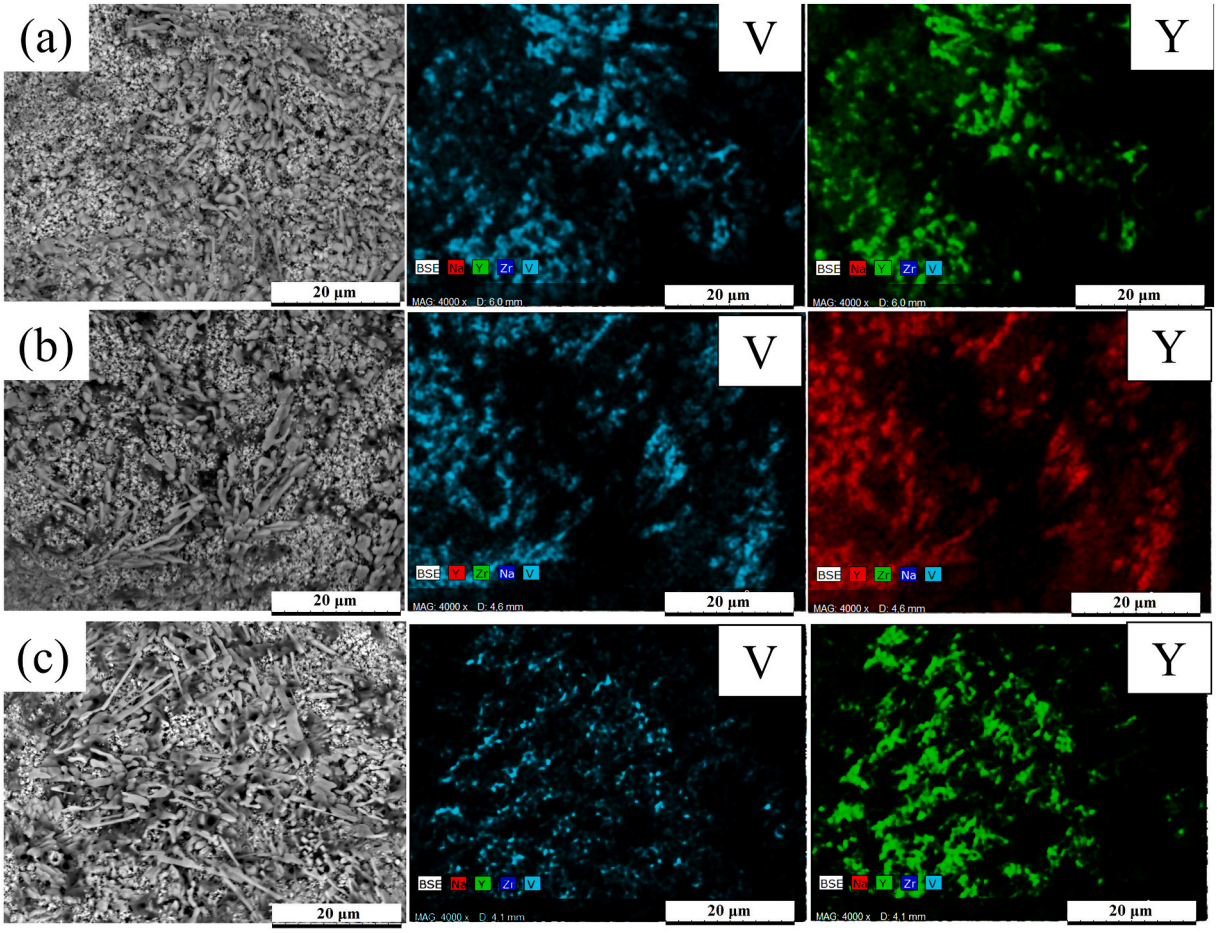

Fig. 8. Top view SEM micrograph of the corroded TBCs and corresponding EDS maps labelled with respective elements (V and Y) for a) C1, b) C2, c) C3.

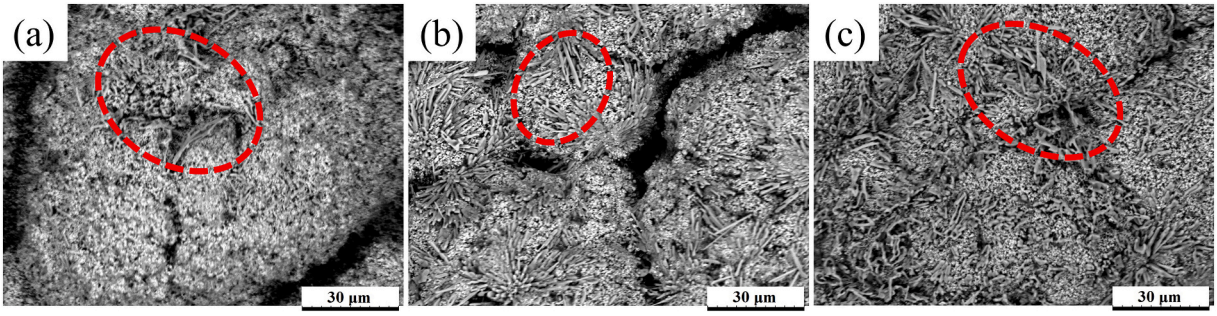

Fig. 9. High magnification top view SEM micrographs of the corroded samples showing corrosion products on (a) C1, (b) C2, and (c) C3.

From the cross-sectional SEM/EDS analysis, it can be seen in Fig. 10 that vanadium from the molten salt composition completely infiltrated all the TBCs, irrespective of their differences in microstructural features. In the columnar microstructured TBCs, different features (columns, column gaps, interconnected pores) respond distinctly to molten salt exposure. For instance, in the column gaps, infiltration occurs without any resistance due to the presence of coarse pores. Additionally, the widening of column gaps due to tensile stresses during the isothermal heating cycle accelerates the corrosive salt infiltration. It should be mentioned that, as the column density increase, the number of column gaps per unit length also increase, which in turn could favor easier infiltration of the corrosive salts. In general, column gaps in the SPS processed TBC act as the weak links in the microstructure when exposed to molten salt. Similar work on the role of column gap in accelerating molten salt infiltration was reported in the literature for gadolinium zirconate-based TBCs [24]. On the other hand, the presence of column gaps in the microstructure was shown to be beneficial in localizing the cracks generated by the erodent and minimized material loss compared to a lamellar microstructured TBC [14]. In the case of within-columns, the molten salt infiltrates through the inter-connected pores in the top coat of the TBCs with relative ease. However, in the absence of inter-connected pores, the molten salt selectively leaches stabilizer content (Y) from the YSZ TBC and forms vanadate, as discussed in the XRD section. During the cooling cycle, the infiltrated salt/corroded product solidifies and contributes to additional strain energy accumulation in the TBC. The accumulated strain energy in the TBC is relieved by creation of new surfaces in form of horizontal delamination cracks, which can be seen in case of C1 (Fig. 11) having highest column density and porosity.

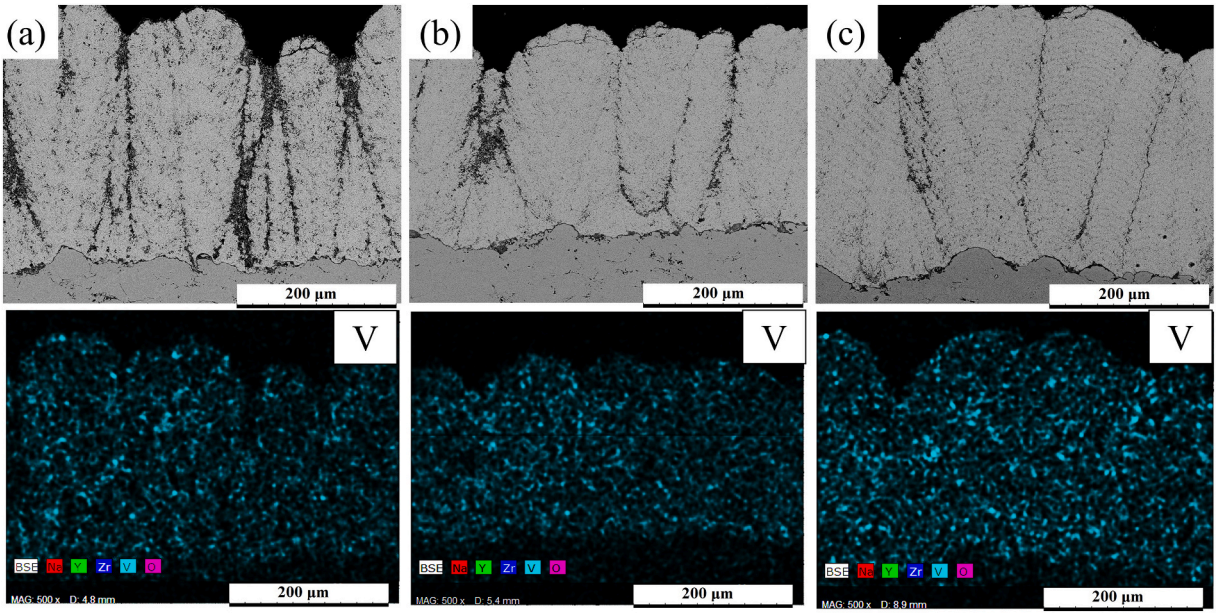

Fig. 10. Cross section SEM micrograph and EDS map showing vanadium infiltration (a) C1, (b) C2, and (c) C3.

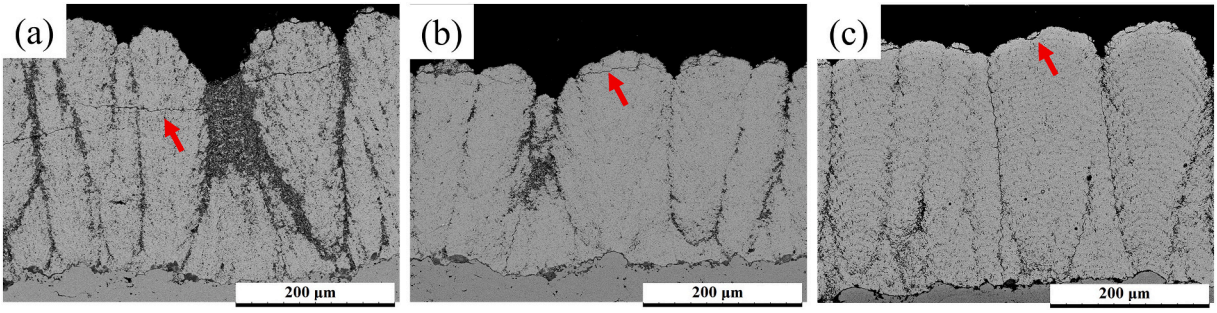

Fig. 11. SEM micrographs of corroded region showing horizontal cracks (a) C1, (b) C2, and (c) C3.

It should be mentioned that the salt infiltration occurs through thickness on long-term exposure and, therefore, precludes 'ranking' in terms of infiltration depth. However, higher column density, smaller column width, wider column gaps in case of C1 make it favorable for the infiltration of the molten salts among the investigated TBCs.

The horizontal cracks in all the TBCs are clearly visible in Fig. 11. In general, the fracture toughness of TBC dictates the capability to withstand the spallation as a result of molten salt attack [7]. Due to the lower fracture toughness of C1 among all the TBCs, it showed delamination cracks across the TBC. Near surface horizontal cracks were also evident in C2 and C3 after corrosion test, according to Fig. 11. However, the extent of damage was comparatively lower in C2 and C3 than C1, which can be attributed to their higher fracture toughness. The post-corrosion analysis results demonstrate that, despite identical corroded phases present and complete corrosive species infiltration, the TBC with higher fracture toughness resists spallation cracks when subjected to molten salt attack.

The XRD results of as-deposited and corroded TBCs are shown in Fig. 12. In the as-deposited TBC samples, Tetragonal (t′) phase of zirconia was observed, as seen in Fig. 12(a). It is desirable to have the tetragonal (t′) zirconia phase, since it is stable in the intended service temperature range without undergoing any undesirable phase transformation [53]. The XRD analysis of the corroded TBCs revealed the presence of monoclinic zirconia as shown in Fig. 8(b). The reaction between the corrosion salts and YSZ resulted in formation of YVO_4, believed to have occurred due to either Eq. (6) or (7) discussed previously. Presence of YVO_4 can also be confirmed from Fig. 12(b).

3.5.1. *Corrosion mechanism*

The schematic illustration of molten salt infiltration mechanism at the onset of hot corrosion test is shown in Fig. 13. Although complete infiltration in all the investigated TBCs was observed, it can be said that the C1 TBC with higher column density, lower column width and higher coarse porosity, due to presence of a greater number of column gaps, aids molten salt infiltration throughout the top coat with relative ease. This can be attributed to the fact that tensile stresses in the TBC during heating cycle accelerate the molten salt infiltration with relative ease through the relatively higher number of column gaps. On the other hand, C2 and C3 TBCs with lower column density, higher column width and lower number of column gaps are relatively more resistant to infiltration through column gap. Additionally, within-columns, lower porosity and minimal interconnected pores are desirable to mitigate molten salt infiltration. In this work, the porosity content within-columns (Class 2, Class 3 and Class 4) was lower for C2 and C3 TBCs compared to C1, as shown in Fig. 3. Furthermore, higher fracture toughness of C2 & C3 than C1 limited post-corrosion damage to near surface cracks in the C2 and C3 TBCs. On the comparison of microstructural features such as column gaps in SPS processed TBCs and lamellar microstructure TBC processed by APS, it is reported that the lamellar microstructured TBC do not permit easy infiltration path for the corrosive species, as seen in the case of columnar SPS TBCs [24,27].

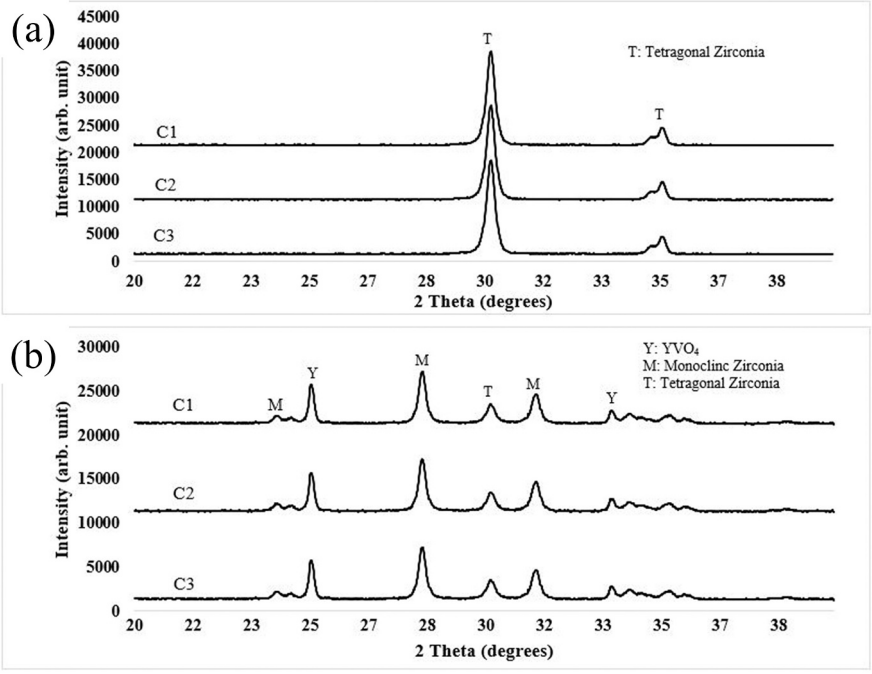

Fig. 12. X-ray diffraction analysis of the TBCs surface (a) before and (b) after corrosion tests.

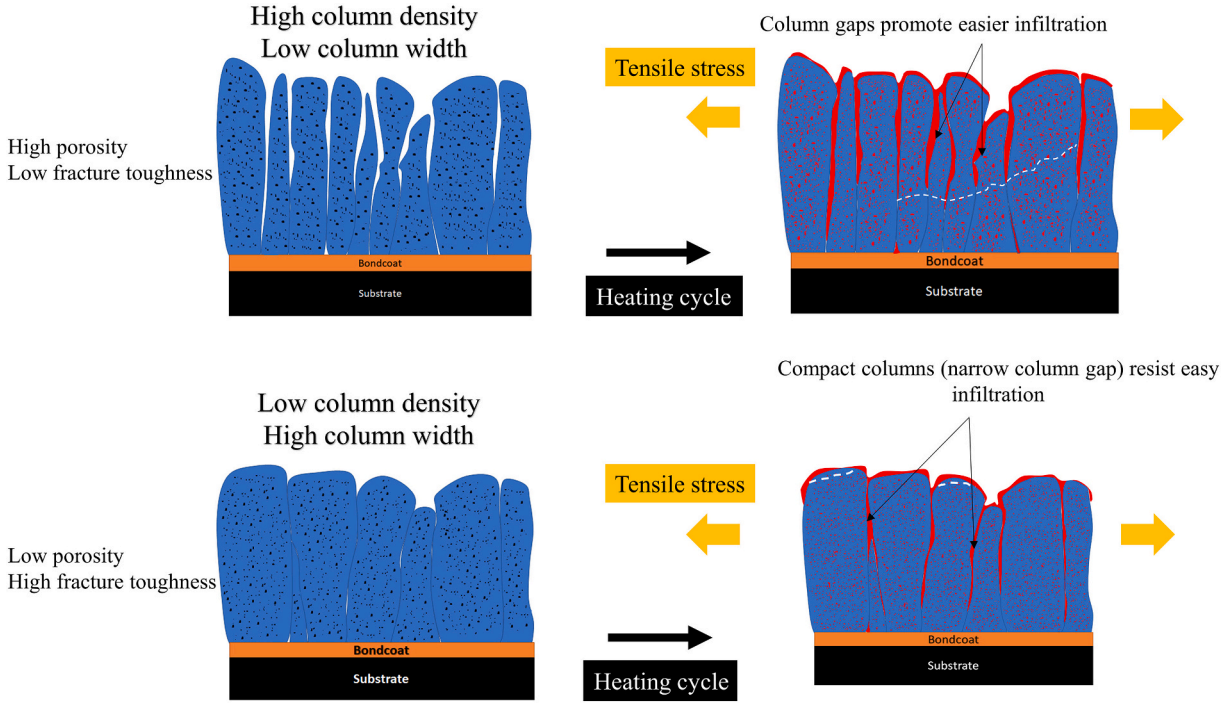

Fig. 13. Proposed hot corrosion mechanism of the TBCs.

3.6. Correlating the microstructure-erosion and corrosion performance

Fig. 14 shows the correlation between total porosity content-fracture toughness-erosion performance of the investigated TBCs. It should be mentioned that the TBCs fracture toughness was evaluated within the columns, which predominantly comprised Class 2, Class 3 and Class 4 porosity along with minimal Class 1 porosity. Among the investigated TBCs, C1 showed higher amount of all porosity classes, which resulted in its highest total porosity content. From Fig. 14, it can be seen that an increase in total porosity content in the case of C1 resulted in inferior fracture toughness compared to C2 and C3 This finding is in agreement with the literature where the TBCs porosity content and its fracture toughness are reported to be inversely proportional [37,43]. Furthermore, fracture toughness of C2 and C3 was comparable, although C2 showed higher total porosity content than C3. Their column density and column width were also comparable, considering the scatter in measurement. It seems that the presence of IP porosity bands in C2 did not compromise its fracture toughness. The mean erosion rate of the investigated TBCs in Fig. 14(b) showed a decreasing trend as the total porosity content decreased, which is in agreement with the literature

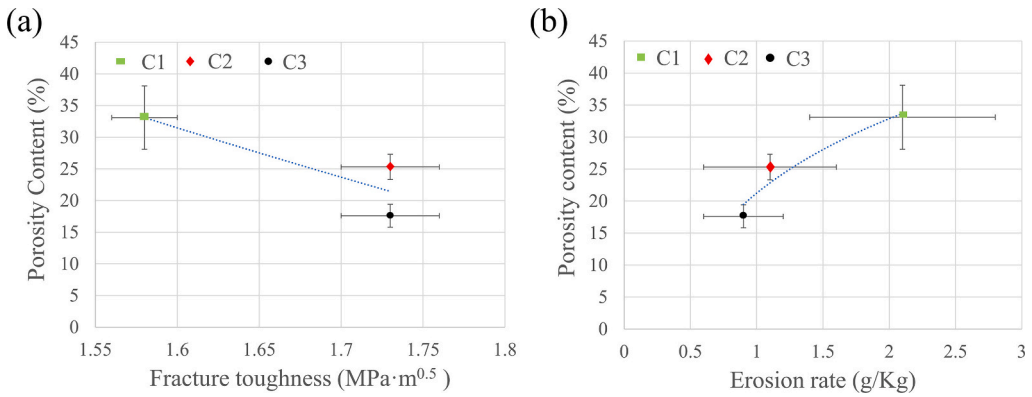

Fig. 14. Porosity content vs. (a) fracture toughness and (b) erosion rate of the investigated TBCs.

[43]. Based on the erosion performance quantification results, it is difficult to point out which porosity class contributed significantly to erosion loss as C1 showed highest porosity across all pore classes. However, from the post-erosion analysis, it was seen that coarse porosity from column gaps was detrimental as they favored easier material removal (tunneling mechanism). Therefore, it can be said that coarse porosity is undesirable in the TBCs to mitigate erosion. In the corrosion test, longer exposure duration disabled the quantification (infiltration depth of corrosive elements) of hot corrosion performance and its correlation to porosity content in the investigated TBCs. However, based on the discussion in post-corrosion analysis, it could be said that a compact columnar TBC microstructure along with low column density (low column gaps) is desirable to mitigate hot corrosion as the column gaps provide easier infiltration path for the molten corrosive salts. Additionally, the presence of IP porosity bands could have assisted in salt penetration due to the fact that they were connected to the column gaps. In general, from this work, it could be said that a compact columnar microstructured TBC with low column density can provide improved damage resistance (corrosion and erosion).

4. Conclusions

This work investigated the influence of microstructural features (porosity, column density, column width) of SPS processed 8YSZ TBCs on erosion and corrosion behavior. The erosion and corrosion results of SPS TBCs were correlated with microstructural features, porosity content, phases, hardness and fracture toughness. Based on the corrosion and erosion results, their mechanisms were proposed. The prominent findings from the study may be summarized as follows:

I. Altering the spray parameters led to distinct microstructural features in the as-deposited TBCs, especially in terms of column density, column width and porosity content, with correspondingly different mechanical properties.
II. It was shown that the TBCs with lower column density, higher column width exhibited improved fracture toughness and enhanced erosion resistance. Furthermore, higher coarse porosity in the deposited SPS processed TBCs, contributed from the column gaps, favored erosion related losses as compared to SPS TBCs with compact columns and lower column density (lower coarse porosity).
III. When exposed to molten salt attack, all the investigated TBCs showed complete infiltration of corrosive salts. Furthermore, phase analysis of the TBCs after corrosion was also identical. However, the damage tolerance of the TBCs due to corrosive species attack was shown to be higher for TBCs with lower column density, higher column width, lower porosity and superior fracture toughness.
IV. For the design of erosion resistant and molten salt attack resistant TBCs, fracture toughness and porosity content are vital, where higher fracture toughness and lower coarse porosity content favors higher durability. It was also shown that, in a columnar microstructured TBCs processed by SPS, microstructural features such as lower column density and high column width are desirable to mitigate erosion and corrosion damage.

CRediT authorship contribution statement

Nitish Kumar: Writing – original draft, Methodology, Investigation, Validation. **Satyapal Mahade:** Supervision, Investigation, Conceptualization, Writing – review & editing. **Ashish Ganvir:** Conceptualization, Writing – review & editing. **Shrikant Joshi:** Methodology, Funding acquisition, Writing – review & editing.

Declaration of competing interest

The authors declare that they have no known competing financial interests or personal relationships that could have appeared to influence the work reported in this paper.

Acknowledgements

The authors gratefully acknowledge help from Mr. Stefan Björklund, University West, Sweden, in spraying the TBCs for this study.

References

[1] R. Vassen, X. Cao, F. Tietz, D. Basu, D. Stöver, Zirconates as new materials for thermal barrier coatings, J. Am. Ceram. Soc. 83 (8) (2000) 2023–2028, https://doi.org/10.1111/j.1151-2916.2000.tb01506.x.
[2] U. Schulz, et al., Some recent trends in research and technology of advanced thermal barrier coatings, Aerosp. Sci. Technol. 7 (1) (Jan. 2003) 73–80, https://doi.org/10.1016/S1270-9638(02)00003-2.
[3] N. Espallargas, Future Development of Thermal Spray Coatings: Types, Designs, Manufacture and Applications, Elsevier, 2015.
[4] A. Ganvir, S. Joshi, N. Markocsan, R. Vassen, Tailoring columnar microstructure of axial suspension plasma sprayed TBCs for superior thermal shock performance, Mater. Des. 144 (Apr. 2018) 192–208, https://doi.org/10.1016/j.matdes.2018.02.011.
[5] T. Patterson, A. Leon, B. Jayaraj, J. Liu, Y.H. Sohn, Thermal cyclic lifetime and oxidation behavior of air plasma sprayed CoNiCrAlY bond coats for thermal barrier coatings, Surf. Coat. Technol. 203 (5) (Dec. 2008) 437–441, https://doi.org/10.1016/j.surfcoat.2008.08.054.
[6] B. Bernard, et al., Thermal insulation properties of YSZ coatings: suspension plasma spraying (SPS) versus electron beam physical vapor deposition (EB-PVD) and atmospheric plasma spraying (APS), Surf. Coat. Technol. 318 (May 2017) 122–128, https://doi.org/10.1016/j.surfcoat.2016.06.010.
[7] S. Gong and Q. Wu, "6 - processing, microstructures and properties of thermal barrier coatings by electron beam physical vapor deposition (EB–PVD)," in Thermal Barrier Coatings, H. Xu and H. Guo, Eds. Woodhead Publishing, 2011, pp. 115–131.
[8] A. Ganvir, N. Curry, S. Bjorklund, N. Markocsan, P. Nylen, Characterization of microstructure and thermal properties of YSZ coatings obtained by axial

suspension plasma spraying (ASPS), J. Therm. Spray Technol. 24 (7) (Jun. 2015) 1195–1204, https://doi.org/10.1007/s11666-015-0263-x.
[9] P.G. Lashmi, P.V. Ananthapadmanabhan, G. Unnikrishnan, S.T. Aruna, Present status and future prospects of plasma sprayed multilayered thermal barrier coating systems, J. Eur. Ceram. Soc. 40 (8) (Jul. 2020) 2731–2745, https://doi.org/10.1016/j.jeurceramsoc.2020.03.016.
[10] Y. Zhao, et al., Porous architecture and thermal properties of thermal barrier coatings deposited by suspension plasma spray, Surf. Coat. Technol. 386 (Mar. 2020), 125462, https://doi.org/10.1016/j.surfcoat.2020.125462.
[11] W. Fan, Y. Bai, Review of suspension and solution precursor plasma sprayed thermal barrier coatings, Ceram. Int. 42 (13) (2016) 14299–14312.
[12] N. Curry, K. VanEvery, T. Snyder, N. Markocsan, Thermal conductivity analysis and lifetime testing of suspension plasma-sprayed thermal barrier coatings, Coatings 4 (3) (Sep. 2014), 3, https://doi.org/10.3390/coatings4030630.
[13] R.S. Lima, B.M.H. Guerreiro, M. Aghasibeig, Microstructural characterization and room-temperature erosion behavior of as-deposited SPS, EB-PVD and APS YSZ-based TBCs, J. Therm. Spray Technol. 28 (1–2) (Jan. 2019) 223–232, https://doi.org/10.1007/s11666-018-0763-6.
[14] S. Mahade, et al., Understanding the effect of material composition and microstructural design on the erosion behavior of plasma sprayed thermal barrier coatings, Appl. Surf. Sci. 488 (Sep. 2019) 170–184, https://doi.org/10.1016/j.apsusc.2019.05.245.
[15] S. Rezanka, D.E. Mack, G. Mauer, D. Sebold, O. Guillon, R. Vaßen, Investigation of the resistance of open-column-structured PS-PVD TBCs to erosive and high-temperature corrosive attack, Surf. Coat. Technol. 324 (Sep. 2017) 222–235, https://doi.org/10.1016/j.surfcoat.2017.05.003.
[16] J.R. Nicholls, M.J. Deakin, D.S. Rickerby, A comparison between the erosion behaviour of thermal spray and electron beam physical vapour deposition thermal barrier coatings, Wear 233–235 (Dec. 1999) 352–361, https://doi.org/10.1016/S0043-1648(99)00214-8.
[17] F. Cernuschi, et al., Solid particle erosion of thermal spray and physical vapour deposition thermal barrier coatings, Wear 271 (11) (Sep. 2011) 2909–2918, https://doi.org/10.1016/j.wear.2011.06.013.
[18] W. Algenaid, A. Ganvir, R.F. Calinas, J. Varghese, K.V. Rajulapati, S. Joshi, Influence of microstructure on the erosion behaviour of suspension plasma sprayed thermal barrier coatings, Surf. Coat. Technol. 375 (Oct. 2019) 86–99, https://doi.org/10.1016/j.surfcoat.2019.06.075.
[19] Z. Chen, S. Speakman, J. Howe, H. Wang, W. Porter, R. Trice, Investigation of reactions between vanadium oxide and plasma-sprayed yttria-stabilized zirconia coatings, J. Eur. Ceram. Soc. 29 (8) (May 2009) 1403–1411, https://doi.org/10.1016/j.jeurceramsoc.2008.09.016.
[20] M.H. Habibi, L. Wang, S.M. Guo, Evolution of hot corrosion resistance of YSZ, Gd2Zr2O7, and Gd2Zr2O7+YSZ composite thermal barrier coatings in Na2SO4+V2O5 at 1050°C, J. Eur. Ceram. Soc. 32 (8) (Jul. 2012) 1635–1642, https://doi.org/10.1016/j.jeurceramsoc.2012.01.006.
[21] R. Vassen, A. Stuke, D. Stöver, Recent developments in the field of thermal barrier coatings, J. Therm. Spray Technol. 18 (2) (2009) 181–186.
[22] A.K. Rai, R.S. Bhattacharya, D.E. Wolfe, T.J. Eden, CMAS-resistant thermal barrier coatings (TBC), Int. J. Appl. Ceram. Technol. 7 (2010) 662–674, https://doi.org/10.1111/j.1744-7402.2009.02373.
[23] C. Batista, A. Portinha, R.M. Ribeiro, V. Teixeira, C.R. Oliveira, Evaluation of laser-glazed plasma-sprayed thermal barrier coatings under high temperature exposure to molten salts, Surf. Coat. Technol. 200 (24) (Aug. 2006) 6783–6791, https://doi.org/10.1016/j.surfcoat.2005.10.011.
[24] S. Mahade, et al., Engineered architectures of gadolinium zirconate based thermal barrier coatings subjected to hot corrosion test, Surf. Coat. Technol. 328 (Nov. 2017) 361–370, https://doi.org/10.1016/j.surfcoat.2017.09.005.
[25] R.G. Wellman, J.R. Nicholls, Erosion, corrosion and erosion–corrosion of EB PVD thermal barrier coatings, Tribol. Int. 41 (7) (Jul. 2008) 657–662, https://doi.org/10.1016/j.triboint.2007.10.004.
[26] S. Mahade, N. Curry, S. Björklund, N. Markocsan, P. Nylén, R. Vaßen, Erosion performance of gadolinium zirconate-based thermal barrier coatings processed by suspension plasma spray, J. Therm. Spray Technol. 26 (1–2) (2017) 108–115.
[27] E. Najafi, Understanding the Effect of Material Composition and Microstructure on the Hot Corrosion Behaviour of Plasma Sprayed Thermal Barrier Coatings, M.S thesis, Division of Subtractive and Additive Manufacturing, University West, Trollhättan, 2019. https://www.diva-portal.org/smash/record.jsf?pid=diva2:1359585.
[28] D. Thirumalaikumarasamy, K. Shanmugam, V. Balasubramanian, Influences of atmospheric plasma spraying parameters on the porosity level of alumina coating on AZ31B magnesium alloy using response surface methodology, Prog. Nat. Sci. Mater. Int. 22 (5) (Oct. 2012) 468–479, https://doi.org/10.1016/j.pnsc.2012.09.004.
[29] A. Ganvir, et al., Influence of microstructure on thermal properties of axial suspension plasma-sprayed YSZ thermal barrier coatings, J. Therm. Spray Technol. 25 (1–2) (2016) 202–212.
[30] S. Mahade, N. Curry, S. Björklund, N. Markocsan, P. Nylén, Thermal conductivity and thermal cyclic fatigue of multilayered Gd2Zr2O7/YSZ thermal barrier coatings processed by suspension plasma spray, Surf. Coat. Technol. 283 (Dec. 2015) 329–336, https://doi.org/10.1016/j.surfcoat.2015.11.009.
[31] ImageJ. https://imagej.nih.gov/ij/.
[32] S. Mahade, R. Li, N. Curry, S. Björklund, N. Markocsan, P. Nylén, Isothermal oxidation behavior of Gd2Zr2O7/YSZ multilayered thermal barrier coatings, Int. J. Appl. Ceram. Technol. 13 (3) (2016) 443–450, https://doi.org/10.1111/ijac.12527.
[33] K. Niihara, R. Morena, D.P.H. Hasselman, Evaluation ofK Ic of brittle solids by the indentation method with low crack-to-indent ratios, J. Mater. Sci. Lett. 1 (1) (1982) 13–16.
[34] N. Curry, K. VanEvery, T. Snyder, J. Susnjar, S. Bjorklund, Performance testing of suspension plasma sprayed thermal barrier coatings produced with varied suspension parameters, Coatings 5 (3) (Sep. 2015), 3, https://doi.org/10.3390/coatings5030338.
[35] A. Ganvir, "Design of Suspension Plasma Sprayed Thermal Barrier Coatings," Ph.D. dissertation, Division of Subtractive and Additive Manufacturing, University West, Trollhättan, 2018, http://urn.kb.se/resolve?urn=urn:nbn:se:hv:diva-12336.
[36] A. Ganvir, N. Curry, S. Govindarajan, N. Markocsan, Characterization of thermal barrier coatings produced by various thermal spray techniques using solid powder, suspension, and solution precursor feedstock material, Int. J. Appl. Ceram. Technol. 13 (2) (2016) 324–332, https://doi.org/10.1111/ijac.12472.
[37] C.S. Ramachandran, V. Balasubramanian, P.V. Ananthapadmanabhan, Erosion of atmospheric plasma sprayed rare earth oxide coatings under air suspended corundum particles, Ceram. Int. 39 (1) (Jan. 2013) 649–672, https://doi.org/10.1016/j.ceramint.2012.06.077.
[38] E.M. Donohue, N.R. Philips, M.R. Begley, C.G. Levi, Thermal barrier coating toughness: measurement and identification of a bridging mechanism enabled by segmented microstructure, Mater. Sci. Eng. A 564 (Mar. 2013) 324–330, https://doi.org/10.1016/j.msea.2012.11.126.
[39] G. Dwivedi, V. Viswanathan, S. Sampath, A. Shyam, E. Lara-Curzio, Fracture toughness of plasma-sprayed thermal barrier ceramics: influence of processing, microstructure, and thermal aging, J. Am. Ceram. Soc. 97 (9) (2014) 2736–2744, https://doi.org/10.1111/jace.13021.
[40] J.W. Murray, G.A. Rance, F. Xu, T. Hussain, Alumina-graphene nanocomposite coatings fabricated by suspension high velocity oxy-fuel thermal spraying for ultra-low-wear, J. Eur. Ceram. Soc. 38 (4) (Apr. 2018) 1819–1828, https://doi.org/10.1016/j.jeurceramsoc.2017.10.022.
[41] D. Zhou, O. Guillon, R. Vaßen, Development of YSZ thermal barrier coatings using axial suspension plasma spraying, Coatings 7 (8) (2017) 120.
[42] H.E. Eaton, R.C. Novak, Particulate erosion of plasma-sprayed porous ceramic, Surf. Coat. Technol. 30 (1) (Jan. 1987) 41–50, https://doi.org/10.1016/0257-8972(87)90006-5.
[43] S. Mahade, A. Venkat, N. Curry, M. Leitner, S. Joshi, Erosion performance of atmospheric plasma sprayed thermal barrier coatings with diverse porosity levels, Coatings 11 (1) (Jan. 2021), 1, https://doi.org/10.3390/coatings11010086.
[44] K.P. Jonnalagadda, et al., Hot corrosion mechanism in multi-layer suspension plasma sprayed Gd 2 Zr 2 O 7/YSZ thermal barrier coatings in the presence of V 2 O 5+ Na 2 SO 4, J. Therm. Spray Technol. 26 (1–2) (2017) 140–149.
[45] P. Mohan, B. Yuan, T. Patterson, V.H. Desai, Y.H. Sohn, Degradation of yttria-stabilized zirconia thermal barrier coatings by vanadium pentoxide, phosphorous pentoxide, and sodium sulfate, J. Am. Ceram. Soc. 90 (11) (2007) 3601–3607, https://doi.org/10.1111/j.1551-2916.2007.01941.x.
[52] S. Bose, S. Bose, Chapter 7–thermal barrier coatings (TBCs), in: High Temp. Coat., 2007, pp. 155–232.
[53] R. Vaßen, M.O. Jarligo, T. Steinke, D.E. Mack, D. Stöver, Overview on advanced thermal barrier coatings, Surf. Coat. Technol. 205 (4) (Nov. 2010) 938–942, https://doi.org/10.1016/j.surfcoat.2010.08.151.